IEEE Access
Multidisciplinary | Rapid Review | Open Access Journal

Received December 1, 2019, accepted December 10, 2019, date of publication December 20, 2019,
date of current version January 14, 2020.

Digital Object Identifier 10.1109/ACCESS.2019.2961247

Near-Field 3D SAR Imaging Using a Scanning Linear MIMO Array With Arbitrary Topologies

BO FAN[1], JING-KUN GAO[2], HONG-JUN LI[1], ZHI-JIE JIANG[1], AND YAN HE[1]
[1]National Innovation Institute of Defense Technology, Academy of Military Sciences, Beijing 100071, China
[2]TH-Satellite Center of China, Beijing 100094, China

Corresponding author: Bo Fan (oceanpearl@126.com)

ABSTRACT For near-field synthetic aperture radar (SAR) imaging, frequency domain imaging algorithms typically require the array elements to be uniformly arranged to facilitate the application of fast Fourier transform (FFT) operations; this greatly restricts the array types that can be used for practical applications. For arrays with non-uniformly positioned antennas, no general and efficient imaging algorithm is available yet. To address this issue, an effective algorithm for efficient three-dimensional (3D) SAR imaging with arbitrary linear multi-input-multi-output (MIMO) array topologies is proposed. Specifically, non-uniform FFT (NUFFT) technology is utilized to tackle the non-uniform sampling issues in both the spatial and the wavenumber domain. Despite the intuitive idea, to achieve satisfied imaging, some issues are non-trivial and should be carefully addressed. Both simulations and experiments show the superiority of the proposed algorithm on computational complexity while maintain the same high imaging precision compared with the back-projection algorithm (BPA). Moreover, we suggest that the concept of NUFFT-based imaging can also be generalized to other imaging regimes with arbitrary array configurations.

INDEX TERMS Radar imaging, multi-input-multi-output, synthetic aperture, array topology, millimeter-wave imaging.

I. INTRODUCTION

Near-field 3D synthetic aperture radar (SAR) imaging, which can look through clothes and wrappers and provide high-resolution images of the target, is a rapidly growing and promising technique for safety inspection, non-destructive testing and so on [1], [2]. By combining a 2D observation aperture and a wideband signal, 3D images with millimeter level resolution can be obtained. Despite this simple general imaging principle, the design of the 2D aperture and the development of the corresponding imaging algorithm are non-trivial tasks [3], [4]. After more than forty years' development since its first demonstration in 1970s [5], different imaging regimes and algorithms have been proposed to meet various kinds of requirements.

One simple way to form a 2D synthetic aperture is a direct extension of the classical SAR geometry to 3D case where a 2D single-input-single-output (SISO) synthetic array is needed. Usually, by compromising system costs and the speed of data acquisition, a scanning 1D transceiver array is used to equivalently achieve this 2D aperture. Actually, this is exactly the imaging system presented in [1] by Pacific Northwest National Laboratory (PNNL). They also demonstrated that the 1D transceiver array can be vertically positioned and scanned in a cylindrical surface to achieve a more stereo illumination of the target [6]. The corresponding imaging algorithms for these SISO-based systems have also been studied by many researchers [7], [8]. In most cases, they can be obtained by generalizing the classical 2D SAR imaging algorithms to 3D cases [9], [10].

In the last decade, multi-input-multi-output (MIMO) techniques started to be widely adopted in near-field 3D SAR imaging [11], [12]. Recently, MIMO-SAR imaging technology is drawing more and more attention as it outperforms previous SISO-SAR imaging systems in several aspects such as higher array utilization efficiency, faster data acquisition speed and better imaging quality [13].

The Quick Personnel Safe (QPS) screening system [14] is a representative that combines MIMO technology with near-field 3D SAR imaging. This system employs a carefully designed "2D-MIMO" topology where transmitters and receivers are installed on a 2D planar panel and no mechanical

The associate editor coordinating the review of this manuscript and approving it for publication was Yang Li.

devices are used. As a result, it could achieve real-time "snapshot" imaging theoretically, and the amount of equivalent phase centers (EPC) this system can form is much larger than the number of its real transmitting and receiving antennas. As a result, the half-wavelength constraint on the space interval of adjacent antenna elements for SISO arrays is no longer necessarily for MIMO arrays. According to [4], current QPS screening system employs the Back Projection Algorithm (BPA), which is notoriously known for its high computational complexity. Without an efficient imaging algorithm, the QPS screening system uses many Graphics Processing Units (GPU) to parallelize and accelerate the imaging process. This greatly raises the system's costs and limits its application. In [15], an efficient frequency domain imaging algorithm for 2D-MIMO was proposed, which can achieve competitive focusing quality compared with BPA while taking much less time. Unfortunately, this algorithm needs the 2D-MIMO array to comply with some specific topologies, and it cannot be used for general 2D-MIMO arrays including the QPS screening system. In [16], a fast imaging algorithm was proposed for real-time imaging. However, this algorithm introduces strong approximations and can hardly be adopted to general imaging geometries.

Other than the MIMO-SAR systems with 2D MIMO arrays mentioned above, there is another popular kind of MIMO-SAR systems where a scanning linear 1D MIMO array is used to form a synthetic 2D observation aperture [12]. In these systems, the data acquisition speed is limited by the mechanical scanning process. However, compared with 2D arrays, much fewer transmitting and receiving antennas are needed, and the system's costs can be greatly decreased. Therefore, these systems are especially suitable for applications such as ground penetrating imaging or non-destructive testing where snap-shot imaging ability is not a necessity. In [12], several basic principles of designing such systems were studied in a comprehensive way. In [11], a fast imaging algorithm built upon far-field beam-forming techniques was proposed. However, the focusing quality is interrelated with the topology of the MIMO array, which means this imaging algorithm cannot be used for more general array designs. In [13], [17], efficient frequency domain imaging algorithms for a scanning linear MIMO array were proposed, which greatly expedite its progress towards practical applications.

As aforementioned, the design of near-field 3D SAR imaging systems is a highly flexible task, especially when combined with MIMO techniques. Different designs have their own advantages or disadvantages and can be suitable for different applications. Consequently, there are many related research topics including system conceptualization, array topology design, imaging algorithms and so on. Beside the system architectures and research progress introduced above, there are also many other interesting works in this field. In [3], [18], efficient wavenumber domain imaging algorithms for cross MIMO arrays were proposed. By utilizing the efficiency of fast Fourier transform (FFT), these algorithms can reduce the imaging time significantly. In [19], [20], the design of

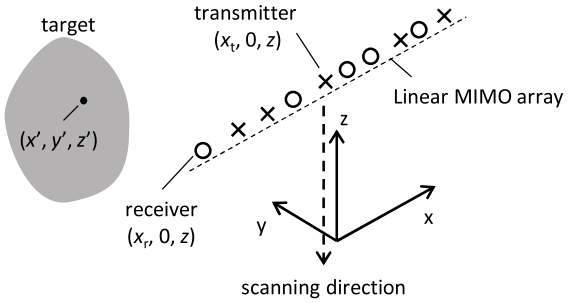

FIGURE 1. The MIMO-SAR imaging geometry with a linear array.

MIMO array topology was studied. As can be seen from these works, for the optimized array topologies, the intervals between array elements are usually unevenly distributed. In [21], [22], metamaterial is introduced into near-field imaging, and MIMO arrays are equivalently achieved using coded metamaterials. For these systems, the image is reconstructed by computational approaches which are rooted on the back-projection principle and regularization methods.

Despite the significant progress that has been made in this area, an obvious incompatibility still exists between current progress on imaging algorithms and array topology design. On one hand, in almost all the literature that focuses on imaging algorithm studies, the array topologies are pre-assumed to satisfy certain specific patterns. For example, one commonly adopted assumption is that either transmitters or receivers are evenly positioned at constant intervals. Consequently, the raw echo data can be efficiently transformed into the wavenumber domain using FFTs, which is the foundation of most wavenumber domain imaging algorithms [23]. On the other hand, optimized array topologies usually feature irregular or non-uniform array elements distributions [20]. As a result, the optimized array topologies and the developed efficient imaging algorithms are largely incompatible with each other at present [24], [25]. In this paper, focusing on the scanning 1D MIMO array regimes, we are trying to fill this gap by proposing an effective algorithm that is compatible with arbitrary linear MIMO array topologies.

To the best of our knowledge, this is the first time that a MIMO-SAR imaging algorithm, which is compatible with arbitrary linear array topologies, is proposed. The paper is organized as follows. In Section 2, the proposed algorithm is presented in detail, including basic formulas, algorithm implementations and the computational complexity analysis. In Section 3, numerical simulations are carried out and quantitative indexes are used to compare the point spread functions (PSF) obtained by different algorithms. In Section 4, two experiments under different configurations are conducted, which comprehensively validate the effectiveness and superiority of the proposed algorithm. Finally, we conclude the paper in Section 5.

II. ALGORITHMS

A. FORMULAS FOR MIMO-SAR IMAGING

The coordinate definitions are illustrated in Figure 1. The linear MIMO array is distributed along the x-axis, while

the y- and z-axis represent the depth direction and scanning direction, respectively. We can see that either transmitters or receivers in Figure 1 are positioned in a non-uniform manner. The simplified echo signal can be modeled as

$$s\left(k, x_{\mathrm{t}}, x_{\mathrm{r}}, z\right)=\iiint o\left(x', y', z'\right) e^{-jkR_{\mathrm{t}}} e^{-jkR_{\mathrm{r}}} \mathrm{d}x' \mathrm{d}y' \mathrm{d}z', \quad (1)$$

where $s(\cdot)$ stands for the echo signal, $o(\cdot)$ stands for the reflectivity distribution, $k = 2\pi/\lambda$ is the wavenumber, and R_{t}, R_{r} represent the distances between the transmitter/receiver and the target, respectively.

By applying a Fourier transform with respect to $x_{\mathrm{t}}, x_{\mathrm{r}}, z$ on both sides of Eq. (1), we can obtain

$$\begin{aligned} &S\left(k, k_{x,t}, k_{x,r}, 2k_z\right) \\ &\quad = \mathrm{FT}_{x_{\mathrm{t}},x_{\mathrm{r}},z}\left[s\left(k, x_{\mathrm{t}}, x_{\mathrm{r}}, z\right)\right] \\ &\quad \approx \iiint o\left(x', y', z'\right) e^{-jk_x x' - jk_y y' - j2k_z z'} \mathrm{d}x' \mathrm{d}y' \mathrm{d}z', \end{aligned} \quad (2)$$

where the approximate equation in the last line is obtained by the spherical wave decomposition theory [13]; the synthetic wavenumber components k_x, k_y are given by

$$\begin{cases} k_x = k_{x,t} + k_{x,r} \\ k_y = k_{y,t} + k_{y,r}, \end{cases} \quad \begin{cases} k_{y,t}^2 = k^2 - k_{x,t}^2 - k_z^2 \\ k_{y,r}^2 = k^2 - k_{x,r}^2 - k_z^2, \end{cases} \quad (3)$$

where $k_{x,t}$, $k_{x,r}$, k_z are the wavenumber domain dual variables corresponding to their spatial domain counterparts $x_{\mathrm{t}}, x_{\mathrm{r}}, z$, respectively.

Given Eq. (2), the target image can be estimated by inverse Fourier transform as follows:

$$\hat{o}\left(x', y', z'\right) = \mathrm{IFT}_{3\mathrm{D}}\left[\hat{O}\left(k_x, k_y, 2k_z\right)\right], \quad (4)$$

where $\hat{O}(\cdot)$ represents the reflection function of the target in the wavenumber domain, which is itself obtained by the following transformation governed by Eq. (3):

$$S\left(k, k_{x,t}, k_{x,r}, 2k_z\right) \rightarrow \hat{O}\left(k_x, k_y, 2k_z\right), \quad (5)$$

In the above formulas, all the variables are presented in the continuous form; however, they become discrete in practice. This means that the implementation of $\mathrm{FT}_{x_{\mathrm{t}},x_{\mathrm{r}},z}[\cdot]$ and $\mathrm{IFT}_{3\mathrm{D}}[\cdot]$ should be carefully considered.

B. IMAGING ALGORITHM FOR ARBITRARY LINEAR MIMO ARRAY TOPOLOGIES

The proposed algorithm can achieve much higher imaging efficiency than BPA, mainly due to the involvement of the $\mathrm{FT}_{x_{\mathrm{t}},x_{\mathrm{r}},z}[\cdot]$ and $\mathrm{IFT}_{3\mathrm{D}}[\cdot]$ operations in Eq. (2) and Eq. (4). For $\mathrm{IFT}_{3\mathrm{D}}[\cdot]$, the sampling positions of $\hat{O}\left(k_x, k_y, 2k_z\right)$ are rarely located on rectangular grids after the transformation in Eq. (2). Therefore, techniques such as Stolt interpolation or NUFFT [26], [27] have been utilized to achieve the transformation from non-uniform wavenumber domain samplings to gridded image data. However, when $\mathrm{FT}_{x_{\mathrm{t}},x_{\mathrm{r}},z}[\cdot]$ is concerned, recent studies have usually solved this problem by avoiding it; for example, replacing $\mathrm{FT}_{x_{\mathrm{t}},x_{\mathrm{r}},z}[\cdot]$ with FFTs by restricting the array elements to be uniformly arranged. In this paper,

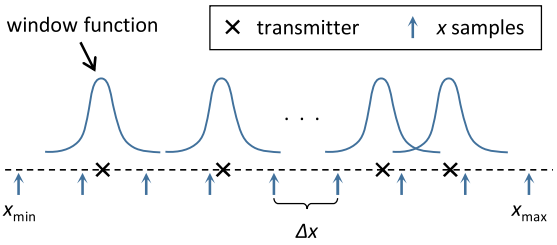

FIGURE 2. The basic idea of a general NUFFT algorithm.

we introduce NUFFTs to $\mathrm{FT}_{x_{\mathrm{t}},x_{\mathrm{r}},z}[\cdot]$ to achieve the transform from non-uniform spatial samplings to wavenumber domain echoes. In this way, the proposed algorithm can be applied to linear MIMO arrays with arbitrary topologies. Since the Fourier transforms with respect to $x_{\mathrm{t}}, x_{\mathrm{r}}, z$ are independent with each other, we take the $\mathrm{FT}_{x_{\mathrm{t}}}[\cdot]$ transformation as an example to illustrate our method. Figure 2 illustrates the basic idea and some key parameters of a general NUFFT algorithm.

From Eq. (3), we know that $k_{x,t}$ is one of the primary variables for imaging and is highly related to NUFFT configurations. According to Figure 2, the sampling interval of $k_{x,t}$ is determined by

$$\Delta k_{x,t} = 2\pi/(x_{\max} - x_{\min}), \quad (6)$$

where $x_{\max}, x_{\min}$ represent the maximum and minimum of the x coordinates of the interpolated uniform samplings, respectively. They should satisfy

$$\begin{cases} x_{\min} < \min x_{\mathrm{t}} \\ x_{\max} > \max x_{\mathrm{t}}, \end{cases} \quad (7)$$

while the residual distance between $x_{\min}$ and $\min x_{\mathrm{t}}$ (or $x_{\max}$ and $\max x_{\mathrm{t}}$) plays the role of zero-padding in the followed FFT. Consequently, we get

$$\begin{aligned} k_{x,t}[n] &= n \cdot \Delta k_{x,t}, \\ n &= \left[-N_{k_{x,t}}/2, N_{k_{x,t}}/2 - 1\right], n \in \mathbb{Z}, \end{aligned} \quad (8)$$

where $N_{k_{x,t}}$ is given by $(x_{\max} - x_{\min})/\Delta x + 1$, Δx is the uniform spatial spacing after interpolation. For convenience, $N_{k_{x,t}}$ is supposed to be an even number in Eq. (8).

To comply with NUFFT algorithm, it is necessary to determine the normalized digital frequency $\Omega_{x,t}$ that corresponds to the non-uniform spatial samplings:

$$\Omega_{x,t}[p] = \mathrm{mod}\left(x_{\mathrm{t}}[p] \cdot \Delta k_{x,t}, 2\pi\right), \; p = 1, 2, \ldots, N_{x,\mathrm{t}}, \quad (9)$$

where $\mathrm{mod}(\cdot, 2\pi)$ represents the modulo operator w.r.t 2π, and $N_{x,\mathrm{t}}$ is the number of transmitters.

In fact, without employing the interpolation shown in Figure 2, the transformation $\mathrm{FT}_{x_{\mathrm{t}}}[\cdot]$ can also be directly implemented by

$$S\left(k_{x,t}[n]\right) = \sum_{p=1}^{N_{x,\mathrm{t}}} s\left(x_{\mathrm{t}}[p]\right) \exp\left(-jx_{\mathrm{t}}[p] \cdot k_{x,t}[n]\right) \quad (10)$$

where n is defined in Eq. (8). However, this direct implementation has a computational complexity of $O\left(N_{x,\mathrm{t}} N_{k_{x,t}}\right)$.

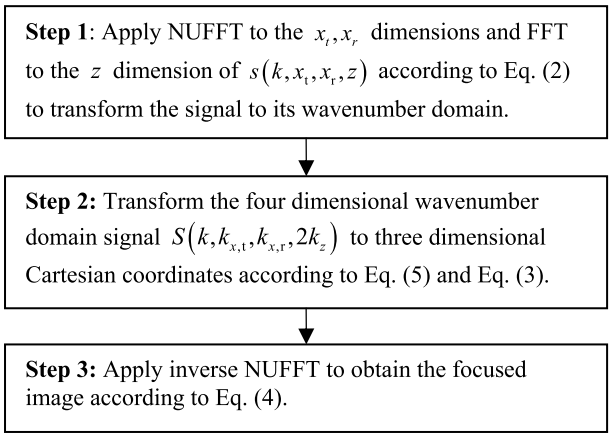

FIGURE 3. The procedures of the proposed MIMO-SAR-NUFFT algorithm.

TABLE 1. Main manipulations and computational complexity of MIMO-SAR-NUFFT.

Manipulations	Computational complexity
NUFFT w.r.t. x_t	$C_1 N_k N_{x,t} N_{x,r} N_z + 5 N_k N_{k_{x,t}} N_{x,r} N_z \log_2 N_{k_{x,t}}$
NUFFT w.r.t. x_r	$C_1 N_k N_{k_{x,t}} N_{x,r} N_z + 5 N_k N_{k_{x,t}} N_{k_{x,r}} N_z \log_2 N_{k_{x,r}}$
FFT w.r.t. z	$5 N_k N_{k_{x,t}} N_{k_{x,r}} N_{k_z} \log_2 N_{k_z}$
Inverse 2D-NUFFT w.r.t. k_x, k_y	$C_2 N_k N_{k_{x,t}} N_{k_{x,r}} N_{k_z} + 5 N_{x'} N_{y'} N_{k_z} (\log_2 N_{x'} + \log_2 N_{y'})$
Inverse FFT w.r.t. k_z	$5 N_{x'} N_{y'} N_{z'} \log_2 N_{z'}$

By contrast, the number of arithmetic operations of a NUFFT implementation of $\mathrm{FT}_{x_t}[\cdot]$ is proportional to [28]

$$N_{k_{x,t}} \cdot \log N_{k_{x,t}} + N_{x,t} \cdot \log\left(\frac{1}{\varepsilon}\right) \tag{11}$$

where ε represents the desired accuracy. More details of the NUFFT algorithms will be introduced in the next section.

For convenience, we can refer to the proposed algorithm as MIMO-SAR-NUFFT, the procedures of which are summarized in Figure 3.

We also conduct a computational complexity analysis of the proposed algorithm, the results are presented in Table 1. In Table 1, $N_k, N_{x,t}, N_{x,r}, N_z$ represent the number of frequency samplings, transmitters, receivers and z-scanning samplings, while $N_{x'}, N_{y'}, N_{z'}$ denote the number of pixels of the expected image along the x-, y- and z-axes, respectively. $N_{k_{x,t}}$ indicates that a $N_{k_{x,t}}$ points FFT is carried out to the x_t-dimension, and $N_{k_{x,r}}$, N_{k_z} are the corresponding FFT parameters to the x_r- and z-dimensions. C_1 refers to the amount of 1D interpolation manipulation calculation for one data point, while C_2 represents the same for 2D interpolation manipulation; note that C_1 and C_2 are constants determined by the required digital precision.

From Table 1, noting that the computational complexities of NUFFT and FFT are of the same order, we can deduce that the computational complexity of the proposed MIMO-SAR-NUFFT is $O(N^4 \log_2 N)$, while that of BPA is $O(N^6)$ [13]. Alternatively, even if the $\mathrm{FT}_{x_t}[\cdot]$ and $\mathrm{FT}_{x_r}[\cdot]$ are implemented directly using Eq. (10), the computational complexity of the proposed algorithm is $O(N^5)$ which is still far lower than that of the BPA. Consequently, from a theoretical perspective, this analysis clearly demonstrates a significant advantage in terms of the efficiency of the proposed algorithm when compared with the gold-standard BPA.

C. DIFFERENT IMPLEMENTATIONS OF NUFFT

As summarized in [29], all existing NUFFTs are essentially based on combining a local interpolation scheme with the standard FFT. In this paper, NUFFT is primarily utilized to realize Fourier transforms from nonequispaced spatial samplings to regularly distributed spectral domain data, which is known as the "type 1" NUFFT [28,30]. The procedure for a typical type 1 NUFFT algorithm is made up of three steps: interpolation, FFT and deconvolution. In the interest of clarity, we here briefly introduce a Gaussian-based NUFFT algorithm as an example.

With the previous definitions in mind, the $\mathrm{FT}_{x_t}[\cdot]$ operator can be implemented as follows. Firstly, an interpolation is carried out in the normalized digital frequency domain:

$$s_\Omega(\Omega_x[q]) = \sum_{p=1}^{N_{x,t}} s_\Omega(\Omega_{x,t}[p]) \cdot g_\varsigma(\Omega_x[q] - \Omega_{x,t}[p]), \tag{12}$$

where $s_\Omega(\Omega_{x,t}[p]) = s(x_t[p])$ and $s_\Omega(\cdot)$ denotes the raw echo data in the normalized digital frequency domain. $g_\varsigma(\cdot)$ is the Gaussian convolution kernel used for interpolation:

$$g_\varsigma(\Omega) = \sum_{l=-\infty}^{+\infty} \exp\left(-\frac{(\Omega - 2l\pi)^2}{\varsigma}\right), \ \Omega \in [0, 2\pi), \tag{13}$$

and $\Omega_x[q]$ represents the uniform sample positions after interpolation:

$$\Omega_x[q] = \frac{2\pi q}{N_{k_{x,t}}}, \quad q = 0, 1, \ldots, N_{k_{x,t}} - 1. \tag{14}$$

Finally, the wavenumber domain signal is obtained using FFT followed by a magnitude modification:

$$S(k_{x,t}[n]) = \frac{1}{G_\varsigma[n]} \cdot \sum_{q=0}^{N_{k_{x,t}}-1} s_\Omega(\Omega_x[q]) \exp\left(-j\frac{2\pi q}{N_{k_{x,t}}} n\right), \tag{15}$$

where $G_\varsigma[n] = \sqrt{2\varsigma}\exp(-n^2\varsigma)$ is the discrete Fourier transform of $g_\varsigma(\Omega)$.

As stated in [31], [32], different NUFFT algorithms differ mainly in terms of their choice of interpolation window function, which governs the tradeoff between accuracy and computational complexity. Normally, a specific NUFFT

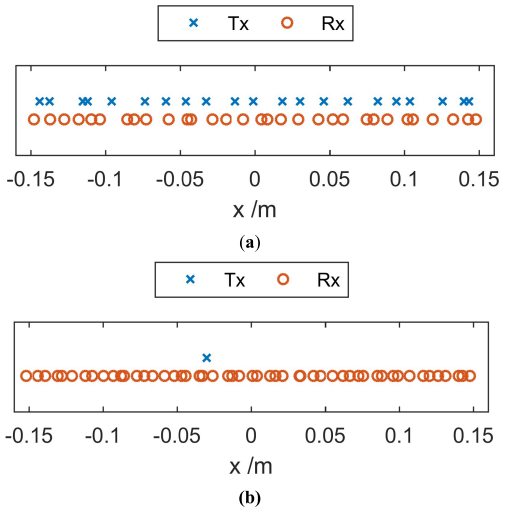

FIGURE 4. Array topologies used for simulation of point targets: (a) Array 1; (b) Array 2.

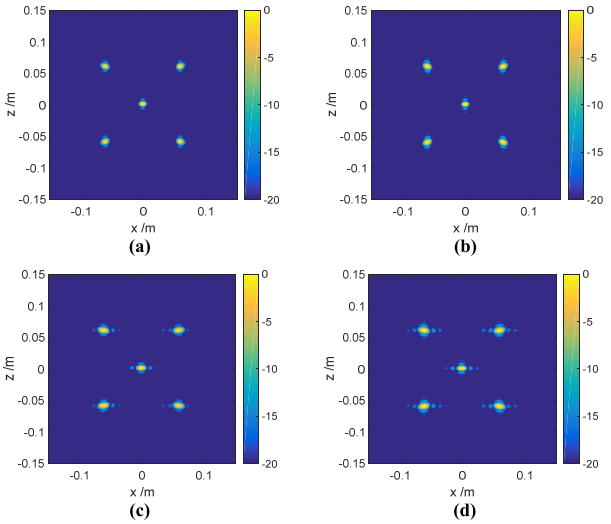

FIGURE 5. Imaging results of different topologies obtained by different algorithms (maximum projections onto the *x*-*z* plane): (a) MIMO-SAR-NUFFT imaging result for Array 1; (b) BPA imaging result for Array 1; (c) MIMO-SAR-NUFFT imaging result for Array 2; (d) BPA imaging result for Array 2.

implementation is not required for the proposed algorithm. Herein, however, the fast Gaussian gridding (FGG) NUFFT is adopted due to its ability to strike a performance balance between interpolation accuracy and computational efficiency [30]. Nevertheless, other NUFFT algorithms can also be adopted, while there may be some differences in time needs or focusing quality.

III. SIMULATIONS

A. IMAGING TESTS WITH DIFFERENT ARRAYS

Two different topologies are used for simulation to facilitate comprehensive validation of the proposed algorithm. As shown in Figure 4, the first array features 21 transmitters and 31 receivers, all of which are non-uniformly distributed. For the second array, a special case is considered in which there are 51 non-uniformly distributed receivers with only one randomly positioned transmitter. In Figure 4, transmitters and receivers are plotted in two different lines so that they can be clearly identified; while in simulations, they are actually in one same line. For the simulation, five ideal scattering points are used as targets. The simulated frequency ranges from 30 GHz to 36 GHz with 31 samplings. The elevation scanning has a 30 cm range with a 3 mm interval, and the distance between the target and the aperture plane is 30 cm.

Imaging results are presented in Figure 5, where BPA results are also presented for comparison. The BPA can be applied to versatile imaging geometries and is also used as the benchmark to validate other algorithms. Note that no side-lobe suppression techniques were used for either algorithm. Within our current implementation of BPA, the B-spline interpolation scheme is utilized. For MIMO-SAR-NUFFT, the accuracy parameter ε of NUFFT is set as 10^{-3} in the simulation.

From Figure 5, we can see that the proposed MIMO-SAR-NUFFT achieves fully focused imaging for both topologies. Moreover, MIMO-SAR-NUFFT is competitive with or even outperforms BPA from the perspective of side-lobe level.

In the interests of presenting a more intuitive analysis of the imaging quality, the point spread function (PSF) of the points in the middle of Figure 5 are extracted and drawn in Figure 6. However, for near field imaging, it is known that the PSF is spatial variant, which can also be clearly observed in Figure 5. Therefore, evaluating the image quality using PSF is only an intuitive and somewhat imprecise manner. It can be seen that the PSFs of the two algorithms are of high consistency. Moreover, quantitative indexes, Peak Side-Lobe Ratio (PSLR) and Integrated Side-Lobe Ratio (ISLR), are calculated and listed in Table 2. For some indexes, the proposed MIMO-SAR-NUFFT algorithm even shows a better performance than BPA. This phenomenon can also be explained by Figure 6. For both array topologies, the level of the first side-lode of MIMO-SAR-NUFFT is obviously lower than that of the BPA in Figure 6. Nevertheless, we want to claim that the PSF has no analytical expression and is very complicate for near field imaging geometries, and its imaging quality assessment is still an open question and cannot be comprehensively represented by one simple index. After all, by examining Figure 5, Figure 6 and Table 2, we can conclude that the proposed MIMO-SAR-NUFFT algorithm is of high imaging accuracy.

In Section II, we have presented that MIMO-SAR-NUFFT exhibits significant advantages in terms of computational complexity when compared with BPA. To validate this, we recorded the time needs of the above simulations and presented the results in Table 3. The two algorithms are implemented under the same hardware and software platforms without using any parallel computing techniques. From

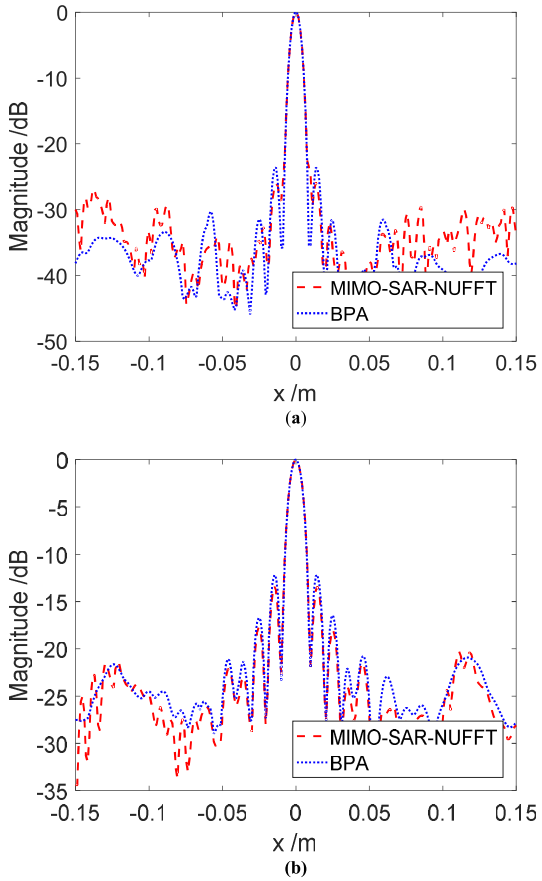

FIGURE 6. PSFs obtained by different algorithms for (a) Array 1 and (b) Array 2.

TABLE 2. Quantitative comparisons of side-lobe performances.

Algorithms	Array 1		Array 2	
	PSLR /dB	ISLR /dB	PSLR /dB	ISLR /dB
MIMO-SAR-NUFFT	-25.867	-17.027	-13.418	-8.305
BPA	-23.627	-18.564	-12.178	-7.153

TABLE 3. Comparisons of the time needs of imaging for different algorithms.

Algorithms	Array 1	Array 2
MIMO-SAR-NUFFT	86.1 s	183.3 s
BPA	16566.9 s	1714.1 s

Table 3, for both arrays, our algorithm shows an advantage of at least one order of magnitude in computing time compared with BPA, which demonstrates good agreement with the results of the theoretical analysis.

B. INFLUENCE OF THE ACCURACY FACTOR ε

As noted above, ε which represents the relative accuracy is a very important factor for NUFFT algorithms [28]. For

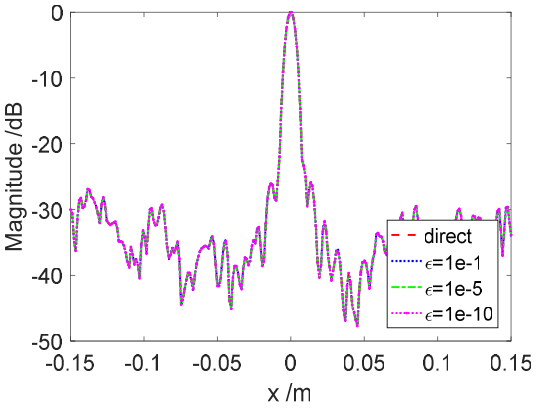

FIGURE 7. PSFs obtained using MIMO-SAR-NUFFT with different εs.

Gaussian-based NUFFT [30], the relationship between some key parameters, e.g. the oversampling rate, the spreading distance and ε, can be analytically expressed. In this section, the impact of ε is analyzed in detail.

We wish to clarify that since the goal of the proposed algorithm is to use NUFFTs to tackle the arbitrary array topology problem, only the ε of the NUFFTs with respect to the x_t- and x_r- dimensions that transform the nonequispaced spatial samplings to regular spectra are studied. This means that all the other parameters in the imaging algorithm remain unchanged.

Different εs are adopted for imaging for Array 1, and the obtained PSFs are plotted in Figure 7. As noted in Section II.B, NUFFT algorithms can be treated as fast approximations of Eq. (10). Therefore, we use the imaging results of the direct implementation to act as the ground-truth. The imaging results with different parameters or implementations are highly similar to those presented in Figure 5. No visual difference can be distinguished and we will not present the figures again here.

It is interesting to note that, as can be seen from Figure 7, the three different εs ranging from 10^{-1} to 10^{-10} all lead to almost the same reconstruction compared with the direct implementation. No difference can be found by checking with the naked eye, and indexes such as PSLR and ISLR also fail to reveal any substantial differences. To conduct a more detailed and quantitative analysis, we define the following relative error for reconstructed images:

$$\varepsilon_{\text{image}} = \frac{\left\|\hat{o}_{\text{direct}} - \hat{o}\right\|}{\left\|\hat{o}_{\text{direct}}\right\|} \tag{16}$$

where $\|\cdot\|$ stands for the L2-norm, $\hat{o}$ is short for the $\hat{o}\left(x', y', z'\right)$ in Eq. (4) which represents the reconstructed image, and $\hat{o}_{\text{direct}}$ denotes the image reconstructed via direct implementation.

From Figure 8, we can see the impact of ε on images more clearly. As ε becomes smaller, the relative image error $\varepsilon_{\text{image}}$ also decreases. However, when the ε is smaller than 10^{-6}, the $\varepsilon_{\text{image}}$ stops declining. This is due to the fact that the $\varepsilon_{\text{image}}$ has touched the lower bound of the precision that a "float" or

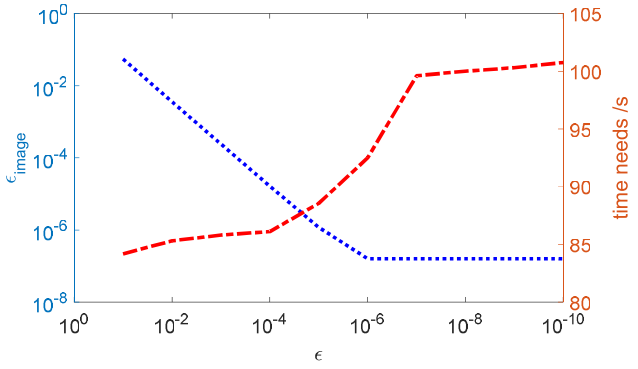

FIGURE 8. Influence analysis of different εs.

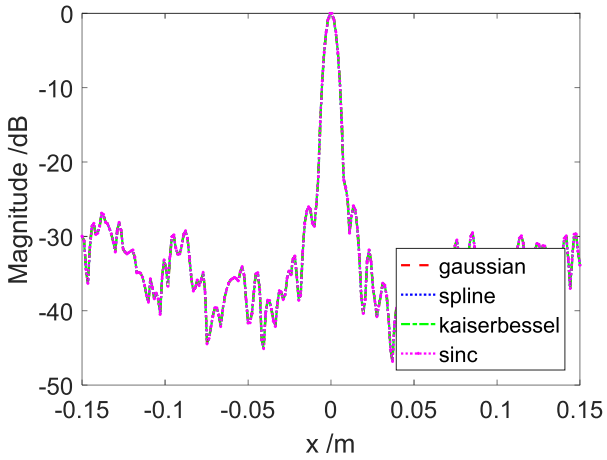

FIGURE 9. PSFs obtained using different NUFFT algorithms.

"single" data type can represent. The time needs data are also plotted in Figure 8. It can therefore be seen that the time needs increase as the ε becomes smaller. Moreover, it is also evident that the variation range of the time needs with different εs only takes up a relative small portion of the total time usage. This is because in our current set up different εs only affect the execution of step one of the algorithm shown in Figure 3, while the remaining two steps take up most of the execution time. According to Figure 8, a preferred value of ε can be selected.

Ultimately, we can see from Figures 7 and 8 that a 10^{-1} level relative error leads to only a tiny difference in the imaging results. Therefore, we conclude that the proposed MIMO-SAR-NUFFT algorithm is not sensitive to the selection of the ε parameter for the current imaging configuration (e.g. frequency band and array topology).

C. INFLUENCE OF DIFFERENT NUFFT ALGORITHMS

As noted above, the main difference between the different NUFFT algorithms concerns their implementation of the interpolation process. Different interpolation schemes can lead to slightly different reconstruction results. However, in the proposed MIMO-SAR-NUFFT algorithm, no specific

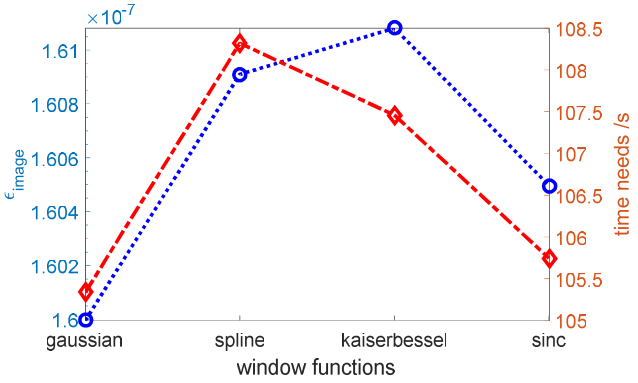

FIGURE 10. Influence analysis of different NUFFT algorithms.

NUFFT or interpolation window function is needed and all methods that can calculate Eq. (10) can potentially be used. In this section, we provide more simulation evidence on this topic.

In addition to the Gaussian window which we employ in previous simulations, several typical window functions including the *B-spline* window [33], *Kaiser-Bessel* window [34] and *sinc* window [35] are chosen for comparison purposes. For the remaing three NUFFT algorithms, we utilized the implementation of the open source library NFFT3 [36].

Array 1 is used to conduct the comparison, and the PSFs obtained using different NUFFT algorithms are presented in Figure 9. From the figure, it can be seen that it is difficult to tell the difference between different algorithms by checking with the naked eye. The PSLR and ISLR of all algorithms are also calculated, while no difference can be observed. Again, we use the $\varepsilon_{\text{image}}$ index defined in Eq. (16) to enable a more detailed comparison. The results and the time needs data are plotted together in Figure 10.

For Figure 10, our aim is to clarify that the *B-spline*-, *Kaiser-Bessel*- and *sinc*- based algorithms are tested using the default parameter settings of the NFFT3 library, and we change the ε factor of the Gaussian-based algorithm to 10^{-13}. We have analyzed that the $\varepsilon_{\text{image}}$ was restricted around 10^{-7} due to the precision of the "float" or "single" data type, while setting ε to 10^{-13} seems redundant. However, after considering both reconstruction precision and efficiency, Gaussian-based NUFFT appears to be a reasonable choice. Above all, we can see that the accuracy and time needs of different NUFFT algorithms differ from each other slightly. All of the above results demonstrate that the choice of NUFFT is not essential for the proposed algorithm.

IV. EXPERIMENTS

Two experiments are carried out to validate the effectiveness of the proposed algorithm. The first one is a proof-of-concept experiment that utilizes a simple target with simple geometry. The second one is conceived with reference to safety inspection applications [37], and a mannequin with a model gun is used as the target.

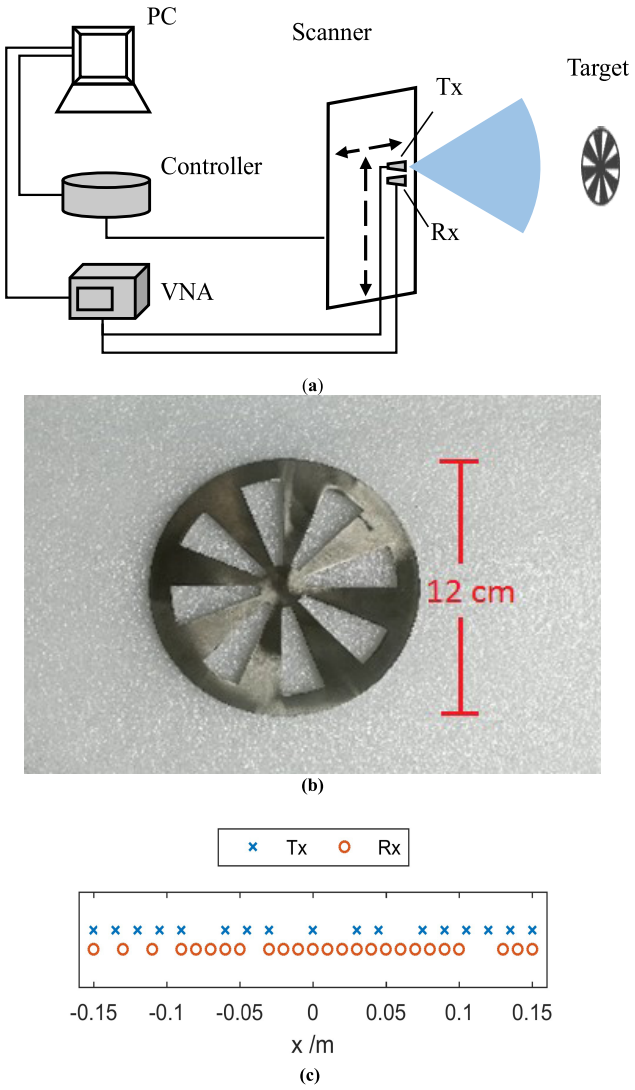

FIGURE 11. Configurations for the first experiment: (a) Experimental schematic diagram; (b) Photograph of the target; (c) Array topology.

A. THE FIRST EXPERIMENT

The experimental setup is illustrated in Figure 11(a). The transmitting and receiving antennas are connected to ports 1 and 2 respectively of the vector network analyzer (VNA). Stepped frequency signals are transmitted and received by the VNA. The "S_{21}" parameter serves as the raw scattering data. The transmitting and receiving antennas are installed on two independent horizontal scanning tracks to equivalently form a 1D MIMO array; these two independent horizontal tracks are then jointly installed on a vertical track to form a planar mechanical scanning apparatus. The VNA, the scanner and the turntable are all connected to and controlled by a personal computer (PC).

As can be seen in Figure 11(b), a lemon-shaped metal piece is used as the target. Configurations for the experiment are the same as those used in the previous simulation except for the array topology. 17 transmitters and 25 receivers are unevenly arranged in a 1D array as shown in Figure 11(c). The total array length is about 30 cm. Imaging results obtained using the proposed algorithm and the BPA are shown in Figure 12.

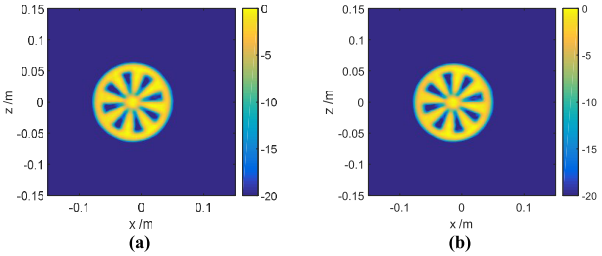

FIGURE 12. Imaging results for the first experiment (maximum projections onto the x-z plane): (a) MIMO-SAR-NUFFT; (b) BPA.

The images are plotted in logarithmic scale with 20 dB dynamic range. Compared with Figure 11(b), we can see that the imaging results in Figure 12 reconstruct the target authentically in both size and shape. The eight "petals" of the target and the little circle with a 2 cm diameter in the middle can be clearly seen. Consequently, we can deduce that the resolution of the obtained image is about 4 mm ($\pi/8$) in the cross-range direction. Comparing Figure 12 (a) and (b), it is difficult to tell the two imaging results apart in a naked-eye manner, which strongly validates the high focusing quality of the proposed algorithm. More importantly, in terms of time needs, the MIMO-SAR-NUFFT requires only 195.1 s while the BPA needs 8033.6 s, which agrees with the precious theoretical analysis and simulation results. The advantage of the MIMO-SAR-NUFFT algorithm in computational efficiency can be clearly seen.

B. THE SECOND EXPERIMENT

For the second experiment, the setup is the same as that shown in Figure 11(a). The target and array topology used in the second experiment are presented in Figure 13.

In this experiment, an array topology is used that incorporates 15 transmitters and 70 receivers, all of which are non-uniformly positioned. The total length of the array is about 60 cm. The experimental frequency ranges from 30 GHz to 36 GHz, with a total of 51 samples and an interval of 120 MHz. The elevation scanning has an 80 cm range with a 4 mm interval, and the distance between the target and the aperture plane is 60 cm.

Imaging results are presented in Figure 14. From this figure, we can see that the image obtained by the proposed MIMO-SAR-NUFFT is very similar to that obtained by BPA. In both images, the model gun is well focused and can be easily recognized. However, when Figure 14 (a) and (b) are compared, some subtle differences between the two images emerge, which is different from the case in Figure 12. We believe that is due to the difference in the targets and array topologies we used for these two experiments. In Figure 12, the target is a simple "lemon" shaped metal plate, which is placed facing the planar observation aperture. Consequently, the main component of the echo data is derived from specular reflection. In Figure 14, the target is far more complicated,

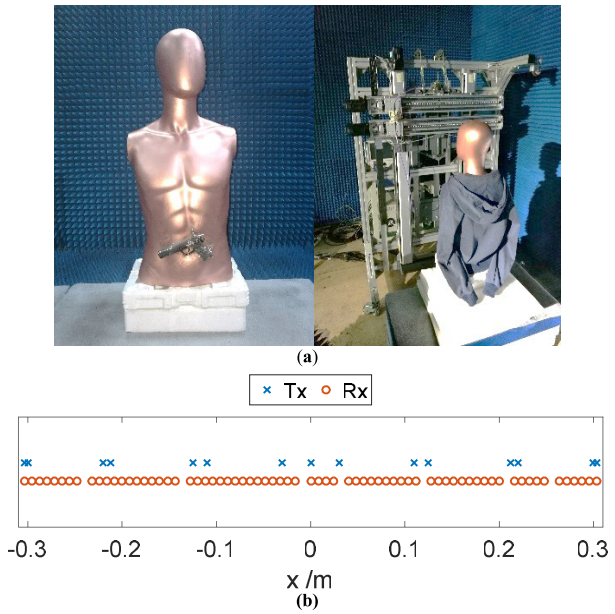

FIGURE 13. Configurations of the second experiment: (a) Photograph of the experimental scenario; (b) Array topology.

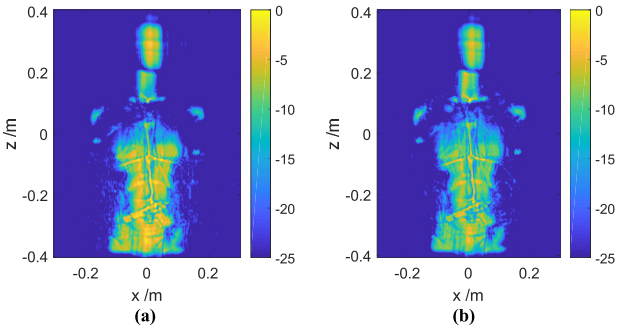

FIGURE 14. Imaging results of the second experiment (maximum projections onto the x-z plane) (a) MIMO-SAR-NUFFT; (b) BPA.

and its echo data is composed of scattered electromagnetic waves due to the different scattering mechanisms in play. Accordingly, the energy distribution of the echo data in the wavenumber domain of the first experiment is more concentrated than is the case for the second experiment. As a result, the difference between the two algorithms is more apparent in the second experiment. Nevertheless, we can see that both algorithms provide high quality imaging results. Moreover, in terms of the time taken to generate the images shown in Figure 14, the proposed MIMO-SAR-NUFFT takes about 553.31 s while the BPA requires 98948.05 s (i.e. about 28 hours). The superior efficiency of the proposed algorithm can thus be clearly seen. In addition, from Section II and Figure 3, we can see that the proposed algorithm is very suitable for parallel implementation. Therefore, we suggest that by parallelizing the current single-thread implementation of the MIMO-SAR-NUFFT algorithm using GPUs, the time needs can be further reduced.

V. CONCLUSION

An imaging algorithm called MIMO-SAR-NUFFT is proposed for near-field 3D SAR imaging with arbitrary linear MIMO array topologies. The NUFFT technology is used to transform the non-uniform array samplings to their wavenumber domain, and also to transform the non-uniform wavenumber domain samplings to the final gridded image data. In this manner, an accurate and efficient imaging algorithm that is capable of tackling arbitrary linear MIMO array topologies is obtained. Detailed description and analysis of the proposed algorithm are provided, and several different simulation and experiments are designed and conducted. Both simulation and experimental results convincingly validate the effectiveness of the proposed algorithm. Finally, we suggest that the proposed NUFFT-based algorithm for arbitrary array topology problem can also be generalized to other similar imaging regimes.

REFERENCES

[1] D. M. Sheen, D. L. McMakin, and T. E. Hall, "Three-dimensional millimeter-wave imaging for concealed weapon detection," *IEEE Trans. Microw. Theory Techn.*, vol. 49, no. 9, pp. 1581–1592, Sep. 2001.
[2] Z. Sun, C. Li, X. Gao, and G. Fang, "Minimum-entropy-based adaptive focusing algorithm for image reconstruction of terahertz single-frequency holography with improved depth of focus," *IEEE Trans. Geosci. Remote Sens.*, vol. 53, no. 1, pp. 519–526, Jan. 2015.
[3] J. Zhou, R. Zhu, G. Jiang, L. Zhao, and B. Cheng, "A precise wavenumber domain algorithm for near range microwave imaging by cross MIMO array," *IEEE Trans. Microw. Theory Techn.*, vol. 67, no. 4, pp. 1316–1326, Apr. 2019.
[4] S. S. Ahmed, A. Schiessl, F. Gumbmann, M. Tiebout, S. Methfessel, and L. Schmidt, "Advanced microwave imaging," *IEEE Microw. Mag.*, vol. 13, no. 6, pp. 26–43, Sep. 2012.
[5] N. H. Farhat and W. R. Guard, "Millimeter wave holographic imaging of concealed weapons," *Proc. IEEE*, vol. 59, no. 9, pp. 1383–1384, Sep. 1971.
[6] D. Sheen, D. McMakin, and T. Hall, "Near-field three-dimensional radar imaging techniques and applications," *Appl. Opt.*, vol. 49, no. 19, pp. E83–E93, 2010.
[7] Z. Sun, C. Li, S. Gu, and G. Fang, "Fast three-dimensional image reconstruction of targets under the illumination of terahertz Gaussian beams with enhanced phase-shift migration to improve computation efficiency," *IEEE Trans. THz Sci. Technol.*, vol. 4, no. 4, pp. 479–489, Jul. 2014.
[8] L. Qiao, Y. Wang, Z. Zhao, and Z. Chen, "Range resolution enhancement for three-dimensional millimeter-wave holographic imaging," *IEEE Antennas Wireless Propag. Lett.*, vol. 15, pp. 1422–1425, 2015.
[9] J. Gao, Y. Qin, B. Deng, H. Wang, and X. Li, "A novel method for 3-D millimeter-wave holographic reconstruction based on frequency interferometry techniques," *IEEE Trans. Microw. Theory Techn.*, vol. 66, no. 3, pp. 1579–1596, Mar. 2018.
[10] Y. Zhang, B. Deng, Q. Yang, J. Gao, Y. Qin, and H. Wang, "Near-field three-dimensional planar millimeter-wave holographic imaging by using frequency scaling algorithm," *Sensors*, vol. 17, no. 10, p. 2438, 2017.
[11] F. Gumbmann and L. Schmidt, "Millimeter-wave imaging with optimized sparse periodic array for short-range applications," *IEEE Trans. Geosci. Remote Sens.*, vol. 49, no. 10, pp. 3629–3638, Oct. 2011.
[12] X. Zhuge and A. G. Yarovoy, "A sparse aperture MIMO-SAR-based UWB imaging system for concealed weapon detection," *IEEE Trans. Geosci. Remote Sens.*, vol. 49, no. 1, pp. 509–518, Jan. 2011.
[13] J. Gao, Y. Qin, B. Deng, H. Wang, and X. Li, "Novel efficient 3D short-range imaging algorithms for a scanning 1D-MIMO Array," *IEEE Trans. Image Process.*, vol. 27, no. 7, pp. 3631–3643, Jul. 2018.
[14] S. S. Ahmed, A. Genghammer, A. Schiessl, and L.-P. Schmidt, "Fully electronic *E*-band personnel imager of 2 m^2 aperture based on a multistatic architecture," *IEEE Trans. Microw. Theory Techn.*, vol. 61, no. 1, pp. 651–657, Jan. 2013.

[15] X. Zhuge and A. G. Yarovoy, "Three-dimensional near-field MIMO array imaging using range migration techniques," *IEEE Trans. Image Process.*, vol. 21, no. 6, pp. 3026–3033, Jun. 2012.
[16] W. F. Moulder, J. D. Krieger, J. J. Majewski, C. M. Coldwell, H. T. Nguyen, D. T. Maurais-Galejs, T. L. Anderson, P. Dufilie, and J. S. Herd, "Development of a high-throughput microwave imaging system for concealed weapons detection," in *Proc. IEEE Int. Symp. Phased Array Syst. Technol. (PAST)*, Oct. 2016, pp. 1–6.
[17] R. Zhu, J. Zhou, G. Jiang, and Q. Fu, "Range migration algorithm for near-field MIMO-SAR imaging," *IEEE Geosci. Remote Sens. Lett.*, vol. 14, no. 12, pp. 2280–2284, Dec. 2017.
[18] R. Zhu, J. Zhou, B. Cheng, Q. Fu, and G. Jiang, "Interpolation-free method for near-field cross MIMO array imaging," *Electron. Lett.*, vol. 54, no. 14, pp. 890–892, Jul. 2018.
[19] K. Tan, S. Wu, Y. Wang, S. Ye, J. Chen, X. Liu, G. Fang, and S. Yan, "On sparse MIMO planar array topology optimization for UWB near-field high-resolution imaging," *IEEE Trans. Antennas Propag.*, vol. 65, no. 2, pp. 989–994, Feb. 2017.
[20] X. Tu, G. Zhu, X. Hu, and X. Huang, "Sparse sequential single-input–multiple-output array design for ultra-wideband radar," *IEEE Antennas Wireless Propag. Lett.*, vol. 14, pp. 1646–1649, 2015.
[21] J. Hunt, T. Driscoll, A. Mrozack, G. Lipworth, M. Reynolds, D. Brady, and D. R. Smith, "Metamaterial apertures for computational imaging," *Science*, vol. 339, no. 6117, pp. 310–313, Jan. 2013.
[22] A. V. Diebold, L. Pulido-Mancera, T. Sleasman, M. Boyarsky, M. F. Imani, and D. R. Smith, "Generalized range migration algorithm for synthetic aperture radar image reconstruction of metasurface antenna measurements," *J. Opt. Soc. Amer. B, Opt. Phys.*, vol. 34, no. 12, pp. 2610–2623, Dec. 2017.
[23] J. Gao, Z. Cui, B. Cheng, Y. Qin, X. Deng, B. Deng, X. Li, and H. Wang, "Fast three-dimensional image reconstruction of a standoff screening system in the terahertz regime," *IEEE Trans. THz Sci. Technol.*, vol. 8, no. 1, pp. 38–51, Jan. 2018.
[24] B. Baccouche, P. Agostini, S. Mohammadzadeh, M. Kahl, C. Weisenstein, J. Jonuscheit, A. Keil, T. Löffler, W. Sauer-Greff, R. Urbansky, P. H. Bolívar, and F. Friederich, "Three-dimensional terahertz imaging with sparse multistatic line arrays," *IEEE J. Sel. Topics Quantum Electron.*, vol. 23, no. 4, Jul./Aug. 2017, Art. no. 8501411.
[25] B. Cheng, Z. Cui, B. Lu, Y. Qin, Q. Liu, P. Chen, Y. He, J. Jiang, X. He, X. Deng, J. Zhang, and L. Zhu, "340-GHz 3-D imaging radar with 4Tx-16Rx MIMO array," *IEEE Trans. THz Sci. Technol.*, vol. 8, no. 5, pp. 509–519, Jul. 2018.
[26] B. Fan, Y. Qin, P. You, and H. Wang, "An improved PFA with aperture accommodation for widefield spotlight SAR imaging," *IEEE Geosci. Remote Sens. Lett.*, vol. 12, no. 1, pp. 3–7, Jan. 2015.
[27] R. Hu, X. Li, T. Yeo, Y. Yang, C. Chi, F. Zuo, X. Hu, and Y. Pi, "Refocusing and zoom-in polar format algorithm for curvilinear spotlight SAR imaging on arbitrary region of interest," *IEEE Trans. Geosci. Remote Sens.*, vol. 57, no. 10, pp. 7995–8010, Oct. 2019.
[28] A. Dutt and V. Rokhlin, "Fast Fourier transforms for nonequispaced data," *SIAM J. Sci. Comput.*, vol. 14, no. 6, pp. 1368–1393, 1993.
[29] J.-Y. Lee and L. Greengard, "The type 3 nonuniform FFT and its applications," *J. Comput. Phys.*, vol. 206, no. 1, pp. 1–5, Jun. 2005.
[30] L. Greengard and J.-Y. Lee, "Accelerating the nonuniform fast Fourier transform," *SIAM Rev.*, vol. 46, no. 3, pp. 443–454, 2004.
[31] A. Capozzoli, C. Curcio, and A. Liseno, "Optimized nonuniform FFTs and their application to array factor computation," *IEEE Trans. Antennas Propag.*, vol. 67, no. 6, pp. 3924–3938, Jun. 2019.
[32] D. R. Prado, M. Arrebola, M. R. Pino, and F. Las-Heras, "An efficient calculation of the far field radiated by non-uniformly sampled planar fields complying Nyquist theorem," *IEEE Trans. Antennas Propag.*, vol. 63, no. 2, pp. 862–865, Feb. 2015.
[33] G. Steidl, "A note on fast Fourier transforms for nonequispaced grids," *Adv. Comput. Math.*, vol. 9, no. 3, pp. 337–352, 1998.
[34] K. Fourmont, "Non-equispaced fast Fourier transforms with applications to tomography," *J. Fourier Anal. Appl.*, vol. 9, no. 5, pp. 431–450, Sep. 2003.
[35] D. Potts, "Schnelle Fourier-transformationen für nichtäquidistante daten und anwendungen," Ph.D. dissertation, Habilitation, Technisch-Naturwissenschaftliche Fakultät, Univ. Lübeck, Lübeck, Germany, 2003.
[36] J. Keiner, S. Kunis, and D. Potts, "Using NFFT 3-A software library for various nonequispaced fast Fourier transforms," *ACM Trans. Math. Softw.*, vol. 36, no. 4, pp. 19-1–19-30, Aug. 2009.
[37] Y. Álvarez, R. Camblor, C. García, J. Laviada, C. Vázquez, S. Ver-Hoeye, G. Hotopan, M. Fernández, A. Hadarig, A. Arboleya, and F. Las-Heras, "Submillimeter-wave frequency scanning system for imaging applications," *IEEE Trans. Antennas Propag.*, vol. 61, no. 11, pp. 5689–5696, Nov. 2013.

BO FAN received the M.S. and Ph.D. degrees from the National University of Defense Technology (NUDT), China, in 2008 and 2014, respectively. He was a Postdoctoral Research with NUDT, from 2015 to 2018. He is currently a Research Assistant with the National Innovation Institute of Defense Technology. His research interests include new regime radar and deep Bayesian learning.

JING-KUN GAO received the B.S. and Ph.D. degrees from the National University of Defense Technology (NUDT), China, in 2013 and 2018, respectively. He is currently with the TH Satellite Center of China, Beijing, China. His research interests include new regime radar, signal processing, and machine learning.

HONG-JUN LI received the M.S. and Ph.D. degrees from the PLA University of Science and Technology, China, in 2013 and 2017, respectively. He is currently a Research Assistant with the National Innovation Institute of Defense Technology. His current research interests include wireless communications and spatial information networks.

ZHI-JIE JIANG received the M.S. degree from the National University of Defense Technology, China, in 2008. He is currently a Research Assistant with the National Innovation Institute of Defense Technology. His research interests include intelligent control system and deep Bayesian learning.

YAN HE received the M.S. degree from Aerospace Engineering University, China, in 1998. He is currently an Associate Research Fellow with the National Innovation Institute of Defense Technology. His research interests include space tracking telemetering and control systems and intelligent data processing.